Molecular Collapse States in Graphene/WSe_2 Heterostructure Quantum Dots

Qi Zheng,[1] Yu-Chen Zhuang,[2] Ya-Ning Ren,[1] Chao Yan,[1] Qing-Feng Sun,[2,3,4,*] and Lin He[1,†]
[1]Center for Advanced Quantum Studies, Department of Physics, Beijing Normal University, Beijing 100875, China
[2]International Center for Quantum Materials, School of Physics, Peking University, Beijing 100871, China
[3]Collaborative Innovation Center of Quantum Matter, Beijing 100871, China
[4]Beijing Academy of Quantum Information Sciences, West Building #3, No. 10 Xibeiwang East Road, Haidian District, Beijing 100193, China

(Received 11 June 2022; revised 16 October 2022; accepted 25 January 2023; published 15 February 2023)

In relativistic physics, both atomic collapse in a heavy nucleus and Hawking radiation in a black hole are predicted to occur through the Klein tunneling process that couples particles and antiparticles. Recently, atomic collapse states (ACSs) were explicitly realized in graphene because of its relativistic Dirac excitation with a large "fine structure constant." However, the essential role of the Klein tunneling in the ACSs remains elusive in experiment. Here we systematically study the quasibound states in elliptical graphene quantum dots (GQDs) and two coupled circular GQDs. Bonding and antibonding molecular collapse states formed by two coupled ACSs are observed in both systems. Our experiments supported by theoretical calculations indicate that the antibonding state of the ACSs will change into a Klein-tunneling-induced quasibound state revealing deep connection between the ACSs and the Klein tunneling.

DOI: 10.1103/PhysRevLett.130.076202

One of the most well-known predictions by quantum electrodynamics is atomic collapse states (ACSs) that are predicted to form when charges of a nucleus exceed 170 [1–3], posing a natural bound on the periodic table of elements. The ACSs are quite similar to the Hawking radiation in black holes since both are predicted to occur accompanied by Klein tunneling [4]. In experiment, realization of the ACSs in a real atom remains a challenge due to the requirement of a highly charged nucleus. Graphene's relativistic Dirac excitation with "small" Fermi velocity $v_F \approx c/300$ (c is the velocity of light in vacuum) makes it an ideal platform to overcome this challenge [5–7], and recently, the ACSs were realized in graphene with a significantly low critical charge [8–11]. Although realizing the ACSs has achieved great success in graphene, the essential role of the Klein tunneling during the formation of the ACSs remains elusive in experiment.

Very recently, the coexistence of the ACSs and the Klein-tunneling-induced quasibound states, i.e., whispering gallery modes (WGMs) [12–20], was demonstrated explicitly in graphene quantum dots (GQDs) with Coulomb-like electrostatic potentials and large cutoff radii [11]. The WGMs originating from the perfect Klein scattering for oblique incidences [14] are essentially different from the ACSs in which electrons with a relatively small angular momentum cannot escape from the Coulomb attractive potential in the supercritical regime [6]. In experiment, the ACSs, which exhibit an exponential energy sequence [6], locate at the center of the potential field due to collapse by the Coulomb potential [8]. However, the WGMs, which are equally spaced in energy, locate at the edge of the potential profile, forming concentric ring structures [14] (see Supplemental Material for details [21]). In this Letter, we systematically study the coupling of two GQDs with Coulomb-like electrostatic potentials. We observe bonding and antibonding molecular collapse states of two coupled ACSs. Our experiments supported by theoretical calculations demonstrate that the antibonding molecular state of the ACSs will change into a WGM, revealing deep connection between the ACSs and the Klein tunneling.

In our experiment, a graphene/WSe_2 heterostructure was obtained by a wet transfer fabrication of a graphene monolayer on freshly exfoliated thick WSe_2 sheets (see Supplemental Material for details [21]). As reported previously, nanoscale WSe_2 QDs were frequently observed at the interface of the graphene/WSe_2 heterostructure [11]. Figure 1(a) shows a representative scanning tunneling microscope (STM) image of an elliptical graphene/WSe_2 heterostructure QD (see Fig. S1 in the Supplemental Material for more experimental data [21]). The thickness of the elliptical QD is 0.8 nm, the same as that of a WSe_2 monolayer. The major and minor diameters of the elliptical QD are about 24.7 and 17.2 nm, respectively. Figure 1(b) shows an atomic-resolved STM image of the heterostructure and its fast Fourier transform (FFT) image. The relative rotation angle between the WSe_2 and graphene is about 26°, and there is no signal of atomic defects and strain structure in the graphene around the elliptical QD. The WSe_2 QDs can introduce Coulomb-like electrostatic potentials on the graphene above them, which generate both the ACSs and WGMs in the GQDs [11]. In a two-dimensional isolated elliptical conductor, the charge density in equilibrium will

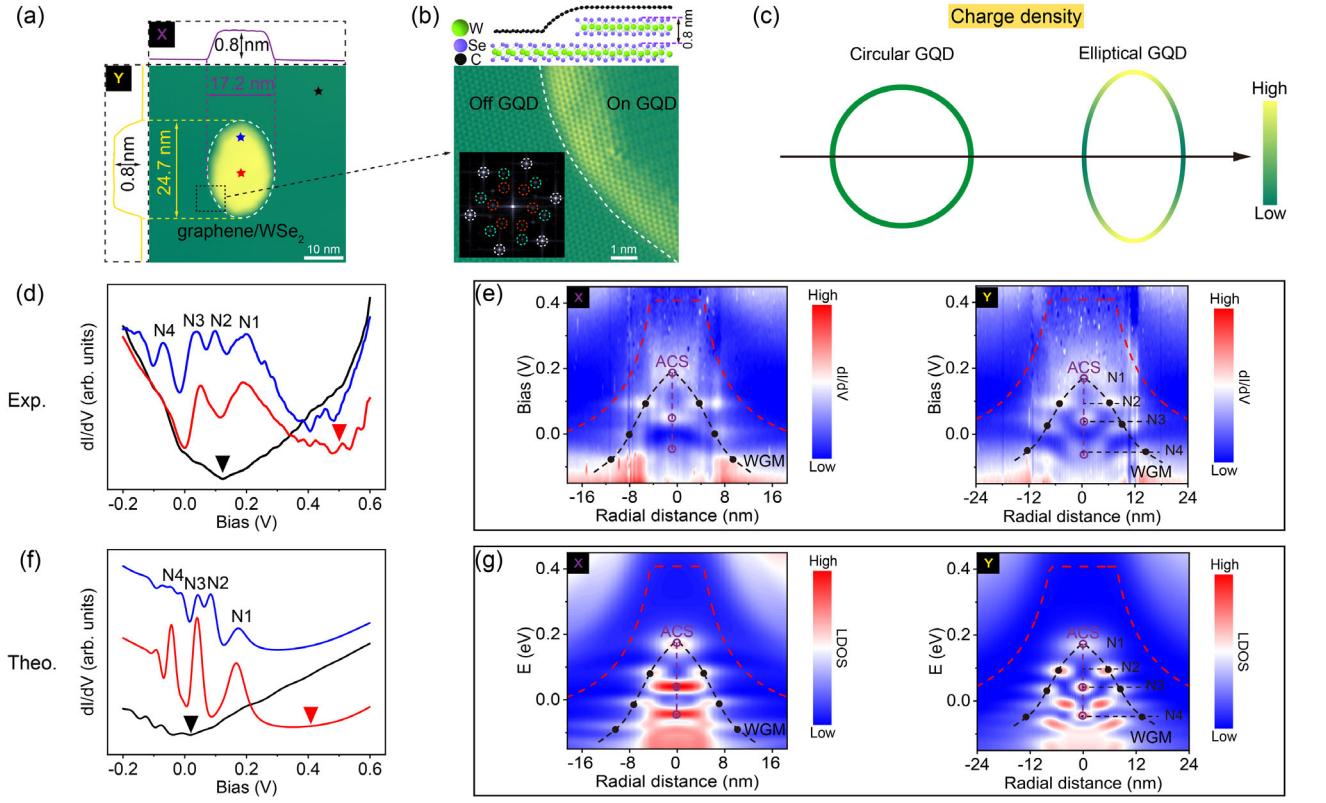

FIG. 1. (a) STM image of an elliptical GQD ($V = 600$ mV, $I = 100$ pA). (b) Top panel: schematic of the heterostructure. Bottom panel: enlargement of the black dashed square of panel (a). Inset of bottom panel: FFT of the heterostructure. The bright spots represent the reciprocal lattice of graphene (white dotted circles), WSe_2 (green dotted circles), moiré structure of the heterostructure (red dotted circles). (c) Calculated charge density distributions for isolated circular and elliptical conductors. (d) Typical dI/dV spectra taken on and off an elliptical GQD. Measured positions of the colored spectra are marked with the corresponding color in panel (a). (e) The radially dI/dV spectroscopic maps along the X axis and Y axis of the elliptical GQD. (f) The calculated LDOS corresponds to (d). (g) The calculated space-energy maps of the LDOS along the X axis and Y axis of the elliptical GQD. The red dashed lines in (e) and (g) indicate Dirac point energy in theory calculation. The black solid (purple hollow) dots indicate the quasibound states via the WGMs (ACSs) confinement.

exhibit a pronounced anisotropy [see Fig. 1(c) and Supplemental Material Fig. S2 [21]], which is expected to strongly affect the confined states.

Figure 1(d) shows three representative STS, i.e., dI/dV, spectra measured around the elliptical GQD. A typical V-shaped spectrum can be observed in graphene off the elliptical GQD with the Dirac point $E_D^{\text{off}} \approx 0.12$ eV, whereas, for the dI/dV spectra measured on the elliptical GQD, the Dirac point is shifted to $E_D^{\text{on}} \approx 0.5$ eV, and a sequence of resonance peaks arising from temporarily confined quasibound states [8–20] are clearly observed. The radially dI/dV spectroscopic maps along the major (Y) and minor (X) axes of the elliptical GQD are shown in Fig. 1(e) (see Figs. S3 and S4 in the Supplemental Material for results in more elliptical GQDs [21]). A significant difference of electrostatic potentials along the two directions can be observed. According to the spatial dependence of the Dirac point E_D obtained from Fig. 1(e) (see Fig. S5 in the Supplemental Material [21]), the confined potential along both the X and Y axes around the elliptical GQDs can be described by a Coulomb-like electrostatic potential:

$$V_{x/y}(r) = \begin{cases} \hbar v_F \frac{\beta_{x/y}}{d_{x/y}}, & r \le d_{x/y}, \\ \hbar v_F \frac{\beta_{x/y}}{r}, & r > d_{x/y}, \end{cases} \tag{1}$$

where $\hbar$ is the reduced Planck constant, r is the distance from the center of GQD, $\beta_{x/y} = Z_{x/y}\alpha$ with $Z_{x/y}$ the number of charges, $\alpha \sim 2.5$ is the fine structure constant of graphene [6], and $d_{x/y}$ is the cutoff radius of the Coulomb potential. By fitting the experimental potential, we obtain $\beta_y = 6$, $d_y = 7.5$ nm in the Y axis and $\beta_x = 3.6$, $d_x = 4.5$ nm in the X axis [Fig. 1(e) and Supplemental Material Fig. S5 [21]]. The anisotropy of the potentials strongly affects the spatial distribution of the quasibound states [Fig. 1(e)]. To explicitly show this, we carry out energy-fixed dI/dV mappings, which reflect spatial distributions of the LDOS, as shown in Figs. 2(a)–2(d) (top panels) (see Fig. S6 in the Supplemental Material for more experimental results [21]). Obviously, they are quite different from that of the circular GQDs [11] and exhibit anisotropic features.

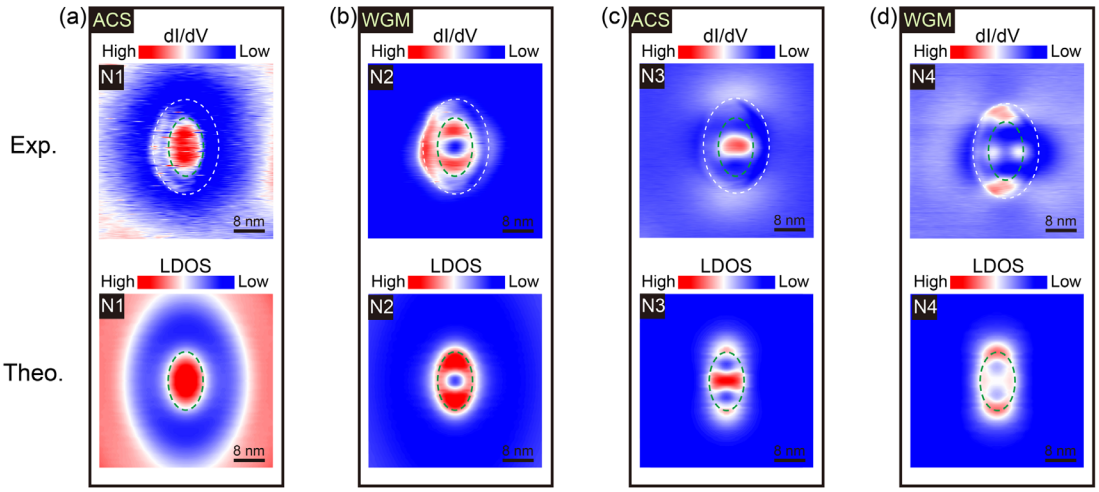

FIG. 2. (a)–(d) Top panels: dI/dV maps at $V_{\mathrm{bias}} = 0.19$ V ($N1$), 0.098 V ($N2$), 0.05 V ($N3$), and −0.05 V ($N4$). N1–N4 are the quasibound states in the elliptical GQD. Bottom panels: calculated LDOS in the elliptical GQD at $E = 0.19$ eV ($N1$), 0.09 eV ($N2$), 0.04 eV ($N3$), and at −0.059 eV ($N4$). The white dashed lines indicate the profile of the elliptical GQD. The green dotted lines indicate the cutoff area of the Coulomb-like electrostatic potential.

To fully understand the electronic properties of the elliptical GQDs, we numerically study the problem with an elliptical Coulomb-like electrostatic potential:

$$V_e(x,y) = \begin{cases} \frac{\hbar v_F \beta_0}{r_0} = \frac{\hbar v_F \beta_x}{d_x} = \frac{\hbar v_F \beta_y}{d_y}, & \sqrt{(x/d_x)^2 + (y/d_y)^2} \le 1, \\ \frac{\hbar v_F \beta_0 / r_0}{\sqrt{(x/d_x)^2 + (y/d_y)^2}}, & \sqrt{(x/d_x)^2 + (y/d_y)^2} > 1. \end{cases} \tag{2}$$

With considering the parameters $\beta_{x/y}$ and $d_{x/y}$ extracted from the experimental results, we obtain theoretical dI/dV spectra [Fig. 1(f)] space-energy maps of the LDOS of the elliptical GQD [Fig. 1(g)], and spatial distributions of the $N1$–$N4$ [Figs. 2(a)–2(d), bottom panels]. Obviously, they are in good agreement with the experimental results. We also calculate the evolution of the quasibound states from the circular GQD to the elliptical GQD to explore their nature (see Figs. S7 and S12 in the Supplemental Material [21]). For a circular GQD, there are both the ACSs and the WGM states [11]. The ACSs locate at the center of the GQD and follow an exponential function in the energy levels. The almost equally-energy-spaced quasibound states at the edge of the GQD are the WGMs (see Figs. S8–S10 in the Supplemental Material for further discussion [21]). The anisotropic elliptical Coulomb potential can be obtained by a smooth transition from a circular Coulomb potential (see Fig. S7 in the Supplemental Material [21]). Here the $N1$ and $N2$ quasibound states in the elliptical GQD evolve from the first ACS and WGM in the circular GQD, respectively. Our results indicate the coexistence of electron WGMs and ACSs in the elliptical GQDs. In our experiment, we can observe Friedel oscillations outside the GQD [11] (see Fig. S11 in the Supplemental Material [21]). Such an effect does not affect the quasibound states in the GQD and is not considered in our calculations. It is interesting to note that the WGMs and the ACSs tend to distribute separately in different regions of the elliptical GQD, which can effectively reduce the Coulomb interaction. This unique space distribution reminds us of the formation of bonding and antibonding molecular states of two coupled quasibound states [17,36,37], suggesting that the WGMs (ACSs) arise from antibonding (bonding) molecular states. Such a result is unexpected because it is believed that the WGMs [12,38] and the ACSs [5–7] have distinct underlying origins.

To further explore the relationship between the WGMs (ACSs) in the elliptical GQD and the antibonding (bonding) molecular states of two coupled GQDs, we systematically study quasibound states of two coupled GQDs, as summarized in Fig. 3. In our experiment, nanoscale monolayer-thick WSe_2 antidots are usually observed around the WSe_2 QDs (Figs. S1 and S13 in Supplemental Material [21]), and the WSe_2 antidot also generates a Coulomb-like potential on the graphene covering it, as shown in Fig. S13 of the Supplemental Material [21]. Therefore, we observe both the WGMs and ACSs in graphene covering the WSe_2 antidot. In our experiment, we can use tip manipulation to move the WSe_2 QD toward the antidot, as shown in Figs. 3(a) and 3(d). Figures 3(b) and 3(c) show the main spectroscopic features of two coupled circular GQDs forming the bonding ($N1$) and antibonding ($N2$) states. Obviously, they are quite different from the quasibound states in an isolated circular GQD. By further increasing the coupling of the two GQDs [Fig. 3(d)], they exhibit quite similar spectroscopic features to that of a single elliptical GQD [see Figs. 2(a), 2(b), and 3(f)]. The differences between the experiment and theory may arise from the deviations of potentials fields in experiment from the ideal elliptic Coulombic potential in theory (see Sec. 9 of

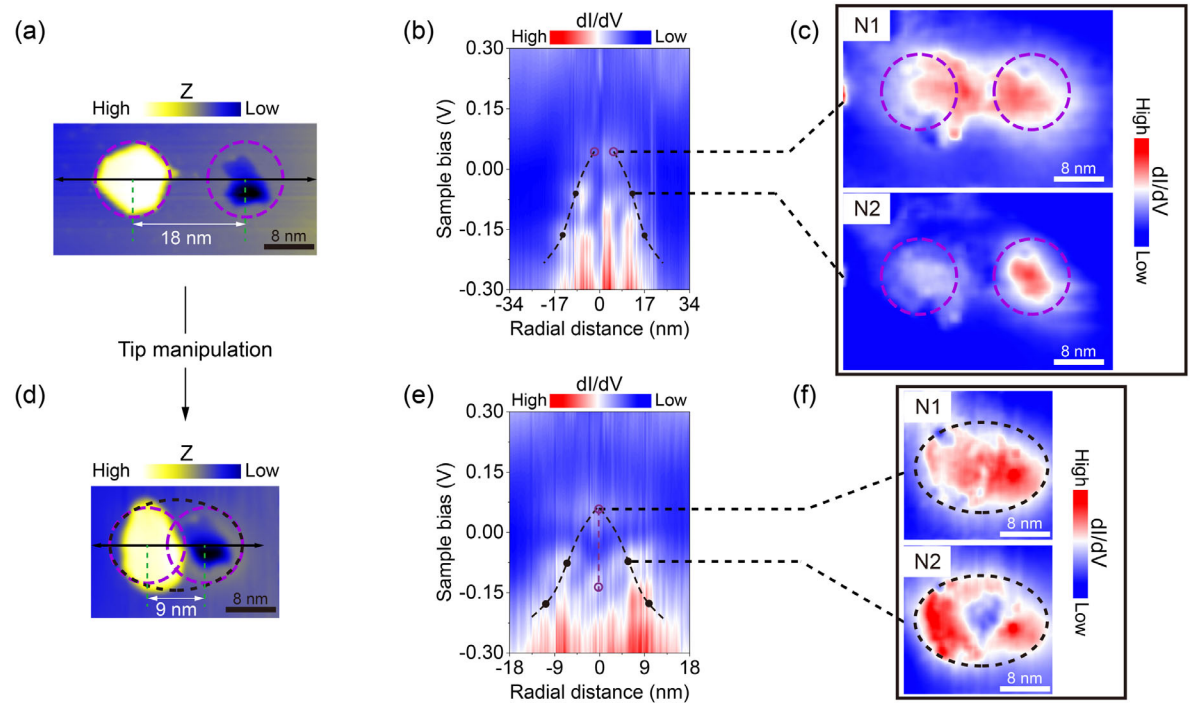

FIG. 3. (a) STM image of two GQDs ($V = 500$ mV, $I = 100$ pA). (b) dI/dV spectroscopic mapping along the black arrow in panel (a). (c) Energy-fixed dI/dV mappings at $N1$ (bonding state) and $N2$ (antibonding state) of the molecular GQD in panel (a). (d) STM image of the two GQDs with a reduced separating distance ~9 nm ($V = 400$ mV, $I = 80$ pA). (e) dI/dV spectroscopic mapping along the black arrow in panel (d). (f) Energy-fixed dI/dV mappings at $N1$ (bonding state) and $N2$ (antibonding state) of the molecular GQD in panel (d).

the Supplemental Material for details [21]). Such a result indicates that the first ACS (WGM) of the elliptical GQD can be viewed as the bonding (antibonding) molecular states of two coupled GQDs.

To further understand our experimental results, we calculate the evolution of quasibound states from a molecular Coulomb potential to the elliptical Coulomb potential. As shown in Fig. 4(a), the molecular Coulomb potential

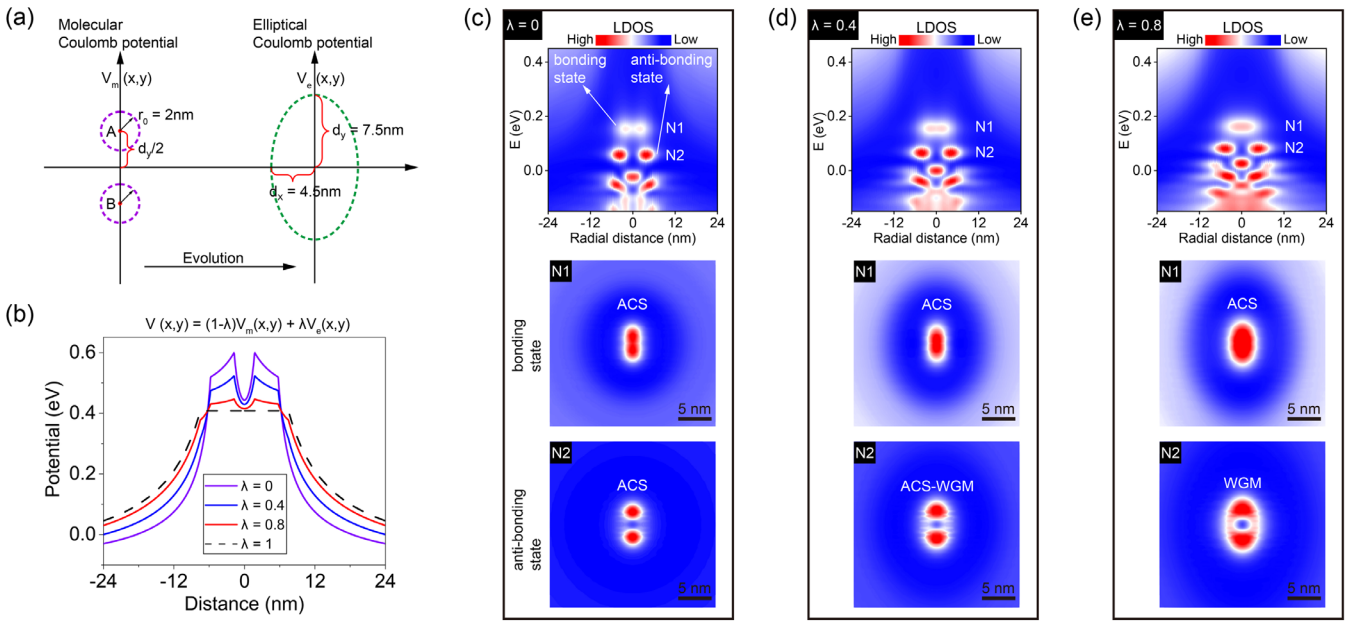

FIG. 4. (a) Configurations of molecular Coulomb potential and elliptical Coulomb potential. (b) Potential profiles of the joint field $V(x, y)$ for different λ. (c)–(e) Top panels: the calculated LDOS space-energy maps along the Y axis of the GQDs. Middle and bottom panels: the corresponding LDOS maps of the first two quasibound states $N1$ and $N2$.

$V_m(x,y)$ is composed of two identical circular Coulomb potentials separated by a distance d_y on the Y axis:

$$V_m(x,y) = V_A(x,y) + V_B(x,y). \tag{3}$$

Here the centers of the two circular potential fields are at $(x,y) = [0,(d_y/2)]$ and $[0,-(d_y/2)]$ (see Supplemental Material for details [21]). When two circular GQDs are closely coupled, the bonding and antibonding states can be obtained using the linear combination of orbitals method, similar to the H_2 molecule [39–41]. Here, the ACSs and WGMs, both of which can be described by quantum numbers (m,n) in a circular GQD, can be also regarded as the electron orbits (see Fig. S9 of the Supplemental Material for the details [21]). Then, they couple to form the bonding and antibonding states, which are spatially redistributed [17,36,37], as shown in Fig. 4(c). The redistributed quasibound states in the molecular GQD appear to be very similar to that in the elliptical GQD. To analyze the relation between the quasibound states in the elliptical GQD and the molecular GQD, we use the potential field $V(x,y) = (1-\lambda)V_m(x,y) + \lambda V_e(x,y)$ with adjustable λ to achieve a smooth evolution from the molecular potential $V_m(x,y)$ to the elliptical potential $V_e(x,y)$, as shown in Fig. 4(b) (the theoretical bulk Dirac point energy is also included in the potential). Figures 4(c)–4(e) display the calculated spatial distribution of the quasibound states in the GQDs with different λ. At $\lambda = 0$, i.e., the standard molecular GQDs, the first two quasibound states correspond to the bonding and antibonding states of the first ACS of each single circular GQD. The bonding state exhibits the LDOS concentrating on the center, while the antibonding state shows the LDOS concentrating on the two ends of the molecular GQDs [Fig. 4(c)]. With increasing λ, the ACS bonding state ($N1$) of the molecular GQDs gradually evolves into the first ACS of the elliptical GQD, and the ACS antibonding state ($N2$) evolves into the first WGM of the elliptical GQD. We would like to mention that higher order ACSs and WGMs experience a similar process. Analogously, the bonding state of WGMs will evolve into the new ACSs, but the antibonding states of WGMs and unbonded WGMs will evolve into the new WGMs (see Fig. S14 in the Supplemental Material for details [21]).

The above calculation strongly supports the results of our experiments (Figs. 2 and 3), revealing deep connection between the ACSs and the Klein tunneling. Actually, the physical origins of the ACSs and WGMs are both related to Klein tunneling and scattering. In the supercritical regime, the electronlike (or holelike) states with a relatively small orbital quantum number $|m+\frac{1}{2}| < |\beta|$ will fall inward toward the center of the GQDs before spiraling back out and coupling to the holelike (electronlike) states to run away through the Klein tunneling (see Supplemental Materials for details [21]). The situation of the WGMs is different. They are quasitrapped by nearly perfect reflections for oblique incidences occurring at the circular p-n junction based on Klein scattering. Hence, although these two types of quasibound states are distinct, it is natural that they could evolve into each other (see Supplemental Material Figs. S16 and S17 along with details and discussion from the perspective of semiclassical particle orbits [21]).

In summary, we systematically study the ACSs and the WGMs in GQDs. Bonding and antibonding molecular collapse states formed by two coupled ACSs are observed. The observed transition between the WGMs and ACSs in this Letter reveals the deep connection between them.

This work was supported by the National Key R&D Program of China (Grants No. 2021YFA1401900, No. 2021YFA1400100, and No. 2017YFA0303301) and the National Natural Science Foundation of China (Grants No. 12141401, No. 11974050, and No. 11921005).

Q. Z. and Y.-C. Z. contributed equally to this work.

*Corresponding author.
sunqf@pku.edu.cn
†Corresponding author.
helin@bnu.edu.cn

[1] Ya. B. Zeldovich and V. S. Popov, Electronic structure of superheavy atoms, Sov. Phys. Usp. **14**, 673 (1972).
[2] W. Greiner, B. Muller, and J. Rafelski, *Quantum Electrodynamics of Strong Fields* (Springer-Verlag, Berlin, 1985).
[3] J. Reinhardt and W. Greiner, Quantum electrodynamics of strong fields, Rep. Prog. Phys. **40**, 219 (1977).
[4] M. K. Parikh and F. Wilczek, Hawking Radiation as Tunneling, Phys. Rev. Lett. **85**, 5042 (2000).
[5] A. V. Shytov, M. I. Katsnelson, and L. S. Levitov, Vacuum Polarization and Screening of Supercritical Impurities in Graphene, Phys. Rev. Lett. **99**, 236801 (2007).
[6] A. V. Shytov, M. I. Katsnelson, and L. S. Levitov, Atomic Collapse and Quasi–Rydberg States in Graphene, Phys. Rev. Lett. **99**, 246802 (2007).
[7] V. M. Pereira, J. Nilsson, and A. H. Castro Neto, Coulomb Impurity Problem in Graphene, Phys. Rev. Lett. **99**, 166802 (2007).
[8] Y. Wang, D. Wong, A. V. Shytov, V. W. Brar, S. Choi, Q. Wu, H.-Z. Tsai, W. Regan, A. Zettl, R. K. Kawakami, S. G. Louie, L. S. Levitov, and M. F. Crommie, Observing atomic collapse resonances in artificial nuclei on graphene, Science **340**, 734 (2013).
[9] J. Mao, Y. Jiang, D. Moldovan, G. Li, K. Watanabe, T. Taniguchi, M. R. Masir, F. M. Peeters, and E. Y. Andrei, Realization of a tunable artificial atom at a supercritically charged vacancy in grapheme, Nat. Phys. **12**, 545 (2016).
[10] Y. Jiang, J. Mao, D. Moldovan, M. R. Masir, G. Li, K. Watanabe, T. Taniguchi, F. M. Peeters, and E. Y. Andrei, Tuning a circular p-n junction in graphene from quantum confinement to optical guiding, Nat. Nanotechnol. **12**, 1045 (2017).
[11] Q. Zheng, Y.-C. Zhuang, Q.-F. Sun, and L. He, Coexistence of electron whispering-gallery modes and atomic collapse

states in graphene/WSe_2 heterostructure quantum dots, Nat. Commun. **13**, 1597 (2022).
[12] A. V. Shytov, M. S. Rudner, and L. S. Levitov, Klein Backscattering and Fabry-Pérot Interference in Graphene Heterojunctions, Phys. Rev. Lett. **101**, 156804 (2008).
[13] Andrea F. Young and Philip Kim, Quantum interference and Klein tunnelling in graphene heterojunctions, Nat. Phys. **5**, 222 (2009).
[14] Y. Zhao, J. Wyrick, F. D. Natterer, J. F. Rodriguez-Nieva, C. Lewandowski, K. Watanabe, T. Taniguchi, L. S. Levitov, N. B. Zhitenev, and J. A. Stroscio, Creating and probing electron whispering-gallery modes in graphene, Science **348**, 672 (2015).
[15] C. Gutiérrez, L. Brown, C.-J. Kim, J. Park, and A. N. Pasupathy, Klein tunnelling and electron trapping in nanometre-scale graphene quantum dots, Nat. Phys. **12**, 1069 (2016).
[16] Z.-Q. Fu, K.-K. Bai, Y.-N. Ren, J.-J. Zhou, and L. He, Coulomb interaction in quasibound states of graphene quantum dots, Phys. Rev. B **101**, 235310 (2020).
[17] Z.-Q. Fu, Y. Pan, J.-J. Zhou, K.-K. Bai, D.-L. Ma, Y. Zhang, J.-B. Qiao, H. Jiang, H. Liu, and L. He, Relativistic artificial molecules realized by two coupled graphene quantum dots, Nano Lett. **20**, 6738 (2020).
[18] K.-K. Bai, J.-J. Zhou, Y.-C. Wei, J.-B. Qiao, Y.-W. Liu, H.-W. Liu, H. Jiang, and L. He, Generating atomically sharp p–n junctions in graphene and testing quantum electron optics on the nanoscale, Phys. Rev. B **97**, 045413 (2018).
[19] J. Lee, D. Wong, J. Velasco Jr, J. F. Rodriguez-Nieva, S. Kahn, H.-Z. Tsai, T. Taniguchi, K. Watanabe, A. Zettl, F. Wang, L. S. Levitov, and M. F. Crommie, Imaging electrostatically confined Dirac fermions in graphene quantum dots, Nat. Phys. **12**, 1032 (2016).
[20] F. Ghahari, D. Walkup, C. Gutiérrez, J. F. Rodriguez-Nieva, Y. Zhao, J. Wyrick, F. D. Natterer, W. G. Cullen, K. Watanabe, T. Taniguchi, L. S. Levitov, N. B. Zhitenev, and J. A. Stroscio, An on/off Berry phase switch in circular graphene resonators, Science **356**, 845 (2017).
[21] See Supplemental Material at http://link.aps.org/supplemental/10.1103/PhysRevLett.130.076202 for more experimental data, analysis, and details of discussion, which includes Refs. [22–35].
[22] H. Eskandari, M. S. Majedi, A. R. Attari, and O. Quevedo-Teruel, Elliptical generalized Maxwell fish-eye lens using conformal mapping, New J. Phys. **21**, 063010 (2019).
[23] D. Moldovan and F. Peeters, PYBINDING v0.9.5: a PYTHON package for tight-binding calculations, Zenodo, 10.5281/zenodo.4010216 (2020).
[24] A. Weiße, G. Wellein, A. Alvermann, and H. Fehske, The kernel polynomial method, Rev. Mod. Phys. **78**, 275 (2006).
[25] L. Convaci, F. M. Peeters, and M. Berciu, Efficient Numerical Approach to Inhomogeneous Superconductivity: The Chebyshev-Bogoliubov–de Gennes Method, Phys. Rev. Lett. **105**, 167006 (2010).
[26] T. L. Le and V. L. Nguyen, Quantitative study of electronic whispering gallery modes in electrostatic-potential induced circular graphene junctions, J. Phys. Condens. Matter **32**, 255502 (2020).
[27] D. Moldovan, M. R. Masir, and F. M. Peeters, Magnetic field dependence of the atomic collapse state in graphene, 2D Mater. **5**, 015017 (2018).
[28] Q. Zheng, M.-H. Zhang, Y.-N. Ren, and L. He, Imaging field-tuned quantum Hall broken-symmetry orders and quantum Hall conducting channel in charge-neutral graphene/WSe_2 heterostructure, arXiv:2112.11654.
[29] E. Mariani, L. I. Glazman, A. Kamenev, and F. V. Oppen, Zero-bias anomaly in the tunneling density of states of graphene, Phys. Rev. B **76**, 165402 (2007).
[30] V. V. Cheianov and V. I. Fal'ko, Friedel Oscillations, Impurity Scattering, and Temperature Dependence of Resistivity in Graphene, Phys. Rev. Lett. **97**, 226801 (2006).
[31] C. Bena, Effect of a Single Localized Impurity on the Local Density of States in Monolayer and Bilayer Graphene, Phys. Rev. Lett. **100**, 076601 (2008).
[32] J. Y. Vaishnav, J. Q. Anderson, and J. D. Walls, Intravalley multiple scattering of quasiparticles in graphene, Phys. Rev. B **83**, 165437 (2011).
[33] Y. Zhang, V. W. Brar, C. Girit, A. Zettl, and M. F. Crommie, Origin of spatial charge inhomogeneity in graphene, Nat. Phys. **5**, 722 (2009).
[34] P. Mallet, I. Brihuega, S. Bose, M. M. Ugeda, J. M. Gomez-Rodriguez, K. Kern, and J. Y. Veuillen, Role of pseudospin in quasiparticle interferences in epitaxial graphene probed by high-resolution scanning tunneling microscopy, Phys. Rev. B **86**, 045444 (2012).
[35] M. Jung, S.-D. Sohn, J. Park, K.-U Lee, and H.-J. Shin, Fingerprints of multiple electron scatterings in single-layer graphene, Sci. Rep. **6**, 22570 (2016).
[36] R. Van Pottelberge, D. Moldovan, S. P. Milovanović, and F. M. Peeters, Molecular collapse in monolayer graphene, 2D Mater. **6**, 045047 (2019).
[37] J. Lu *et al.*, Frustrated supercritical collapse in tunable charge arrays on graphene, Nat. Commun. **10**, 477 (2019).
[38] M. I. Katsnelson, K. S. Novoselov, and A. K. Geim, Chiral tunnelling and the Klein paradox in graphene, Nat. Phys. **2**, 620 (2006).
[39] W. Heitler and F. London, Wechselwirkung neutraler Atome und homoopolare Bindung nach der Quantenmechanik, Z. Phys. **44**, 455 (1927).
[40] J. E. Lennard-Jones, The electronic structure of some diatomic molecules, Trans. Faraday Soc. **25**, 668 (1929).
[41] R. S. Mulliken, Spectroscopy, molecular orbitals, and chemical bonding, Science **157**, 13 (1967).